A Search for New Exotic Particles with Jets in Proton-Proton Collisions at the CMS Experiment

---

Dissertation

zur

Erlangung der naturwissenschaftlichen Doktorwürde
(Dr. sc. nat.)

vorgelegt der

Mathematisch-naturwissenschaftlichen Fakultät

der

Universität Zürich

von

Johnny B. Goode

aus

Deutschland

Promotionskommission

Prof. Dr. Ben Kilminster (Vorsitz)

Prof. Dr. Florencia Canelli

Prof. Dr. Nicola Serra

Prof. Dr. Gino Isidori

Zürich, 20...

1

Abstract

The Standard Model of particle physics has been very successful. But there are problems. They can be explained by new exotic particles.

A search is presented for a new exotic particle. Events with jets are considered. A novel technique is used. The search is based on Run-2 proton-proton collision data at a center-of-mass energy of 13 TeV recorded with the CMS detector corresponding to an integrated luminosity of $137.1\,\mathrm{fb}^{-1}$.

Upper limits are set on the production cross section of a new exotic particle as a function of mass. Results are compared with theoretical predictions to obtain lower limits on the mass. At 95% confidence level, new exotic particles are excluded for masses below X GeV.

12

Acknowledgements

I want to thank the great people in the UZH group and at CMS Collaboration that have helped me along the way, and with whom it was a great privilege and pleasure to work on diverse projects and push the limits of our understanding of Nature.

Special thanks go to my supervisor, Prof. Dr. ...; my supervisor Dr. ...; ...

I would also like to thank my parents and family, for supporting me along my studies.

Contents

1 Introduction

Over the last 100 years, physicists have made large strides in understanding the natural laws that govern the universe as we know it. The Standard Model (SM) of particle physics describes matter and its interactions.

In 2012, the discovery of the Higgs boson was announced by the ATLAS and CMS experiments [1–3] at CERN's LHC. The Higgs was 47 years before that [4, 5]. Despite its many successes, there are both theoretical and experimental reasons that imply the SM is not the final theory of Nature.

This dissertation has the following structure: Chapter 2 discusses the SM, after which Chapter 3 motivates the search for new hypothetical particles. Chapter 4 describes the LHC accelerator, CMS detector and the data collection. Chapter 5 describes the physics objects that are relevant for this thesis. After these, Chapter 7 discusses the selections.

2 The Standard Model

This chapter introduces the Standard Model (SM) of particle physics. I left a bit of text with equations, citations, figures, and tables as an example of this template.

2.1 The Standard Model

A rough timeline of the experimental discovery of particles is given by Fig. 2.1. More detailed historical discussions can be found in Refs. [6–8].

With a mass of $m_\mathrm{t} \approx 172.8\,\mathrm{GeV}$ [10, p. 32], the top quark is by far the heaviest fermion.

The discovery of the Higgs was announced in 2012 [1–3, 11]. A single Higgs boson is the simplest and most minimal solution, although it is possible to achieve SBB with more than one Higgs boson. No evidence of additional Higgs bosons have been found so far [12].

2.1.1 The Standard Model Lagrangian

The SM is encoded in the *SM Lagrangian density.* The terms of the Lagrangian density can be grouped into three separate *sectors*:

$$\mathcal{L}_\mathrm{SM} = \mathcal{L}_\mathrm{gauge} + \mathcal{L}_\mathrm{Higgs} + \mathcal{L}_\mathrm{Yukawa}. \tag{2.1}$$

Secondly, the SM is a *gauge theory*: It has an internal symmetry that corresponds to the local $\mathrm{SU}(3)_\mathrm{C} \times \mathrm{SU}(2)_\mathrm{L} \times \mathrm{U}(1)_\mathrm{Y}$ symmetry group. The SM gauge group is spontaneously broken to

$$\mathrm{SU}(3)_\mathrm{C} \times \mathrm{SU}(2)_\mathrm{L} \times \mathrm{U}(1)_\mathrm{Y} \xrightarrow{\mathrm{SSB}} \mathrm{SU}(3)_\mathrm{C} \times \mathrm{U}(1)_\mathrm{EM} \tag{2.2}$$

by the nonzero vev of the Higgs field, where $\mathrm{U}(1)_\mathrm{EM}$ is the gauge symmetry group for QED.

2.1.2 The gauge sector

The gauge sector can be written as

$$\mathcal{L}_\mathrm{gauge} = \sum_f \sum_{\psi_f} \overline{\psi}_f i\gamma^\mu D_\mu \psi_f - \frac{1}{4} G^a_{\mu\nu} G_a^{\mu\nu} - \frac{1}{4} W^i_{\mu\nu} W_i^{\mu\nu} - \frac{1}{4} B^{\mu\nu} B^{\mu\nu}, \tag{2.3}$$

in natural units $c = \hbar = 1$ [14], and where $a = 1, ..., 8$ and $i = 1, 2, 3$. In the first term, matter is given by five fermion fields ψ_f in three generations $f = 1, 2, 3$;

$$Q^f_\mathrm{L} = \begin{pmatrix} u^f_\mathrm{L} \\ d^f_\mathrm{L} \end{pmatrix}, \quad u^f_\mathrm{R}, \quad d^f_\mathrm{R}, \quad L^f_\mathrm{L} = \begin{pmatrix} \nu^f_\mathrm{L} \\ e^f_\mathrm{L} \end{pmatrix}, \quad e^f_\mathrm{R}. \tag{2.4}$$

Their Dirac adjoints are given by $\overline{\psi}_f = \psi^\dagger_f \gamma^0$.

The covariant derivative

$$D_\mu = \partial_\mu + i g_\mathrm{s} t_a G^a_\mu + i g T_i W^i_\mu + i g' \frac{Y}{2} B_\mu \tag{2.5}$$

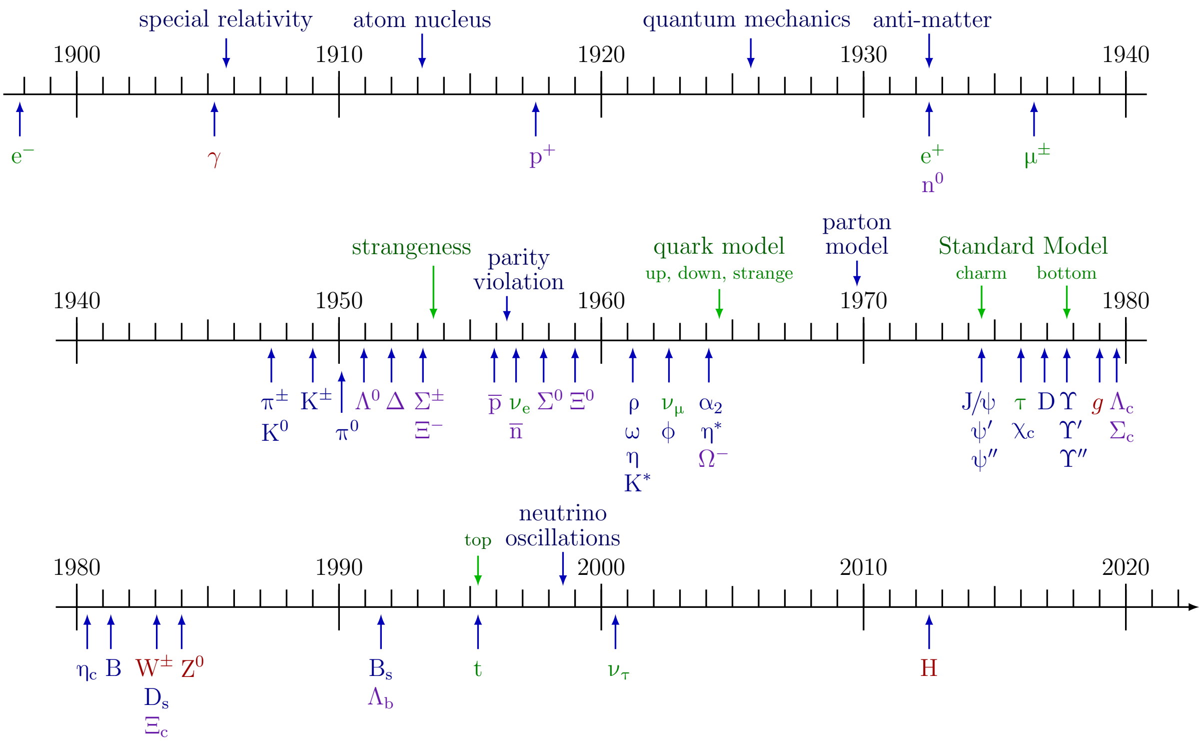

Figure 2.1: A timeline of particle physics in the last 130 years. Adapted from Ref. [9].

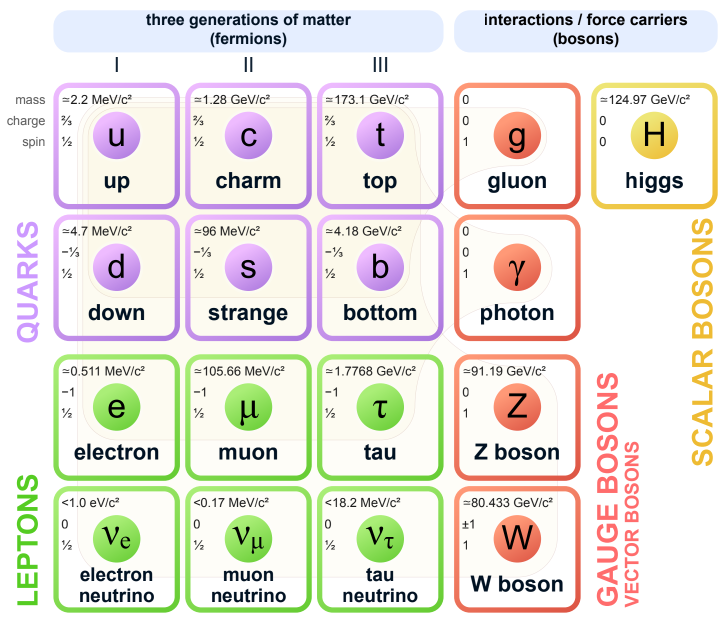

Figure 2.2: A table of the particles in Standard Model of particle physics and their properties. Figure taken from Ref. [13].

Table 2.1: Summary of the representation and quantum numbers SM fields. Bold numbers indicate the dimension of the representation under the respective gauge group.

Field name	Symbol	Representations		Quantum numbers		
		$\mathrm{SU}(3)_\mathrm{C}$	$\mathrm{SU}(2)_\mathrm{L}$	T_3	$Y/2$	$Q = T_3 + Y/2$
Quark doublet	$Q_\mathrm{L} = \begin{pmatrix} u_\mathrm{L} \\ d_\mathrm{L} \end{pmatrix}$	**3**	**2**	$\begin{pmatrix} +\frac{1}{2} \\ -\frac{1}{2} \end{pmatrix}$	$+\frac{1}{6}$	$\begin{pmatrix} +\frac{2}{3} \\ -\frac{1}{3} \end{pmatrix}$
Up-quark singlet	u_R	**3**	**1**	$+\frac{2}{3}$	$+\frac{2}{3}$	$+\frac{2}{3}$
Down-quark singlet	d_R	**3**	**1**	$-\frac{1}{3}$	$-\frac{1}{3}$	$-\frac{2}{3}$
Lepton doublet	$L_\mathrm{L} = \begin{pmatrix} \nu_\mathrm{L} \\ e_\mathrm{L} \end{pmatrix}$	**1**	**2**	$\begin{pmatrix} +\frac{1}{2} \\ -\frac{1}{2} \end{pmatrix}$	$-\frac{1}{2}$	$\begin{pmatrix} 0 \\ -1 \end{pmatrix}$
Lepton singlet	e_R	**1**	**1**	0	-1	-1
Gluon field	G^a_μ	**8**	**1**	0	0	0
Weak gauge field	$W^i_\mu = \begin{pmatrix} W^+_\mu \\ W^-_\mu \\ W^3_\mu \end{pmatrix}$	**1**	**3**	$\begin{pmatrix} +1 \\ -1 \\ 0 \end{pmatrix}$	0	$\begin{pmatrix} +1 \\ -1 \\ 0 \end{pmatrix}$
Hypercharge field	B_μ	**1**	**1**	0	0	0
Higgs doublet	$\Phi = \begin{pmatrix} \phi^+ \\ \phi^0 \end{pmatrix}$	**1**	**2**	$\begin{pmatrix} +\frac{1}{2} \\ -\frac{1}{2} \end{pmatrix}$	$+\frac{1}{2}$	$\begin{pmatrix} +1 \\ 0 \end{pmatrix}$
Conjugate Higgs doublet	$\Phi^\mathrm{c} = \begin{pmatrix} \phi^{0*} \\ \phi^- \end{pmatrix}$	**1**	**2**	$\begin{pmatrix} +\frac{1}{2} \\ -\frac{1}{2} \end{pmatrix}$	$-\frac{1}{2}$	$\begin{pmatrix} 0 \\ -1 \end{pmatrix}$

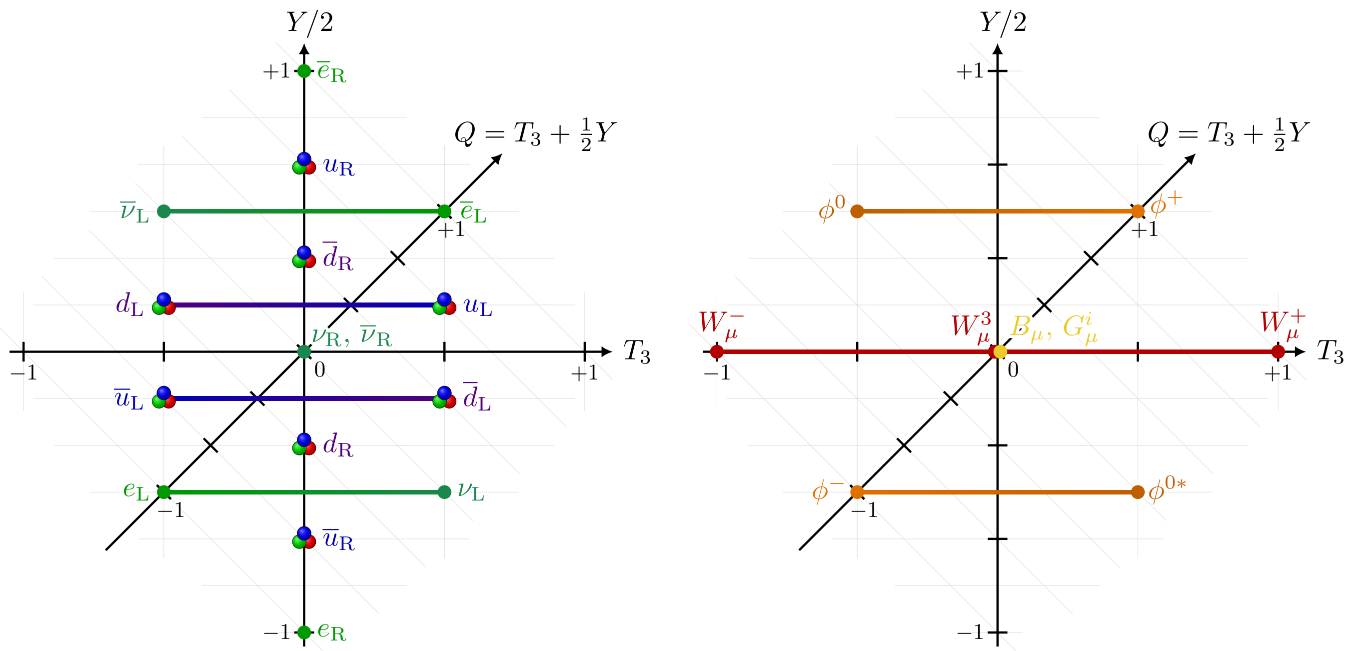

Figure 2.3: Graph of the $(T_3, Y/2)$ quantum numbers.

where T_i and t_a and are the generators for $\mathrm{SU}(2)_\mathrm{L}$ and $\mathrm{SU}(3)_\mathrm{C}$, respectively, and Y is the weak hypercharge of the field that D_μ acts on.

Through the Higgs mechanism, the gauge bosons acquire mass and mix into the mass eigenstates

$$W_\mu^\pm = \frac{W_\mu^1 \mp i W_\mu^2}{\sqrt{2}}, \quad Z_\mu = W_\mu^3 \cos\theta_\mathrm{W} + B_\mu^3 \sin\theta_\mathrm{W}, \quad A_\mu = W_\mu^3 \sin\theta_\mathrm{W} - B_\mu^3 \cos\theta_\mathrm{W}, \tag{2.6}$$

where $W_\mu^\pm$ are the charged W boson fields, Z_μ is the neutral Z boson field, A_μ is the photon field, and θ_W is the Weinberg angle given by $\sin\theta_\mathrm{W} = g'/\sqrt{g^2 + g'^2}$. After mixing, the new covariant derivative becomes

$$D_\mu = \partial_\mu + i g_\mathrm{s} t_a G_\mu^a + i\frac{g}{\sqrt{2}} T^+ W_\mu^+ + i\frac{g}{\sqrt{2}} T^- W_\mu^- + i\frac{g}{\cos\theta_\mathrm{W}} \left(T_3 - \sin^2\theta_\mathrm{W}\, Q\right) Z_\mu + ieQA_\mu, \tag{2.7}$$

with ladder operators $T^\pm = T_1 \pm i T_2$.

2.1.3 The Yukawa sector

In order to explain mass of the fermions,

$$\mathcal{L}_\mathrm{Yukawa} = -Y_d^{fg} \overline{Q}_\mathrm{L}^f \Phi d_\mathrm{R}^g - Y_u^{fg} \overline{Q}_\mathrm{L}^f \Phi^\mathrm{c} u_\mathrm{R}^g - Y_e^{fg} \overline{L}_\mathrm{L}^f \Phi e_\mathrm{R}^g + \text{h.c.}, \tag{2.8}$$

with the conjugate Higgs doublet $\Phi^\mathrm{c} = i\sigma_2 \Phi^\dagger$, and unitary Yukawa matrices Y_d^{fg}, Y_u^{fg}, $Y_e^{fg} \in \mathrm{U}(3)$ that mixes the fermion generations. As Φ is a scalar field that forms a weak isospin doublet,

$$\Phi = \begin{pmatrix} \phi^+ \\ \phi^0 \end{pmatrix}. \tag{2.9}$$

Because the Higgs vev is nonzero, we can fix the $\mathrm{SU}(2)_\mathrm{L}$ gauge. It is convenient to choose the unitary gauge

$$\Phi = \frac{1}{\sqrt{2}} \begin{pmatrix} 0 \\ v + h \end{pmatrix}, \tag{2.10}$$

with the vev $v \approx 246\,\mathrm{GeV}$, a real constant, and the neutral Higgs field h, a (real) scalar. Therefore, after SSB, we are left with

$$\mathcal{L}_\mathrm{Yukawa} = -\frac{Y_d^{fg}}{\sqrt{2}} \overline{d}_\mathrm{L}^f (v+h) d_\mathrm{R}^g - \frac{Y_u^{fg}}{\sqrt{2}} \overline{u}_\mathrm{L}^f (v+h) u_\mathrm{R}^g - \frac{Y_e^{fg}}{\sqrt{2}} \overline{e}_\mathrm{L}^f (v+h) e_\mathrm{R}^g + \text{h.c.} \tag{2.11}$$

2.1.4 CKM matrix

To explain the suppressed decay rate of $\mathrm{K}^0 \to \mu^+\mu^-$, Glashow, Iliopoulos, and Maiani used a mixing matrix and proposed the existence of the charm quark [15]. This is referred to as the *Glashow–Iliopoulos–Maiani* (GIM) *mechanism*. The mixing of two quark generations is given by the *Cabibbo matrix*:

$$\begin{pmatrix} d' \\ s' \end{pmatrix} = \begin{pmatrix} \cos\theta_\mathrm{C} & \sin\theta_\mathrm{C} \\ -\sin\theta_\mathrm{C} & \cos\theta_\mathrm{C} \end{pmatrix} \begin{pmatrix} d \\ s \end{pmatrix}, \tag{2.12}$$

where $|d'\rangle$ and $|s'\rangle$ represent the weak eigenstates, which are linear combinations of the mass eigenstates $|d\rangle$ and $|s\rangle$. The mixing is quantified with the *Cabibbo angle* $\theta_\mathrm{C} \approx 13.04°$.

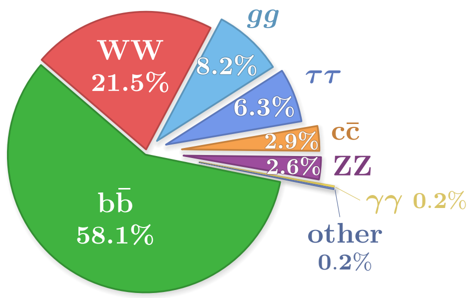

Figure 2.4: Pie chart of Higgs branching fractions.

The mixing of three generations is given by

$$\begin{pmatrix} d' \\ s' \\ b' \end{pmatrix} = \begin{pmatrix} V_{ud} & V_{us} & V_{ub} \\ V_{cd} & V_{cs} & V_{cb} \\ V_{td} & V_{ts} & V_{tb} \end{pmatrix} \begin{pmatrix} d \\ s \\ b \end{pmatrix}, \tag{2.13}$$

where the matrix is the so-called *Cabbibo-Kobayashi-Maskawa* (CKM) *matrix*, denoted by V_{CKM}.

2.2 Higgs

A pie chart of Higgs decay can be found in Fig. 2.4.

2.3 The physics of proton-proton collisions

The substructure of the proton has been carefully studied in deep inelastic scattering (DIS) experiments at SLAC [16, 17] and DESY [18], which collided electrons or positrons with protons.

In the parton model, *parton distribution functions* (PDFs) describe the probability of finding a parton of type p with momentum fraction x in a collision at some momentum scale Q as a function of the form $f_p(x, Q^2)$ [19–23]. The proton has *valence quarks* and *sea quarks*. To reflect the proton quantum numbers, the PDFs are normalized:

$$\int_0^1 \left[f_{\mathrm{u}}(x, Q^2) - f_{\bar{\mathrm{u}}}(x, Q^2) \right] \mathrm{d}x = 2, \qquad \int_0^1 \left[f_{\mathrm{d}}(x, Q^2) - f_{\bar{\mathrm{d}}}(x, Q^2) \right] \mathrm{d}x = 1. \tag{2.14}$$

This follows from the factorization theorem [25, 26], which provides a formula to calculate the cross sections of a hard process with an integral of the form

$$\sigma(\mathrm{pp} \to X + Y) = \sum_{i,j} \int_0^1 \int_0^1 f_i(x_1, Q^2) f_j(x_2, Q^2) \hat{\sigma}_{ij \to X}(x_1, x_2, Q^2)\, \mathrm{d}x_1\, \mathrm{d}x_2\,, \tag{2.15}$$

where $\sigma_{ij \to X}(x_1, x_2, Q^2)$ is the parton-level cross section of the hard process, $i + j \to X$, and parton i (j) carries a fraction x_1 (x_2) of the momentum of its mother proton.

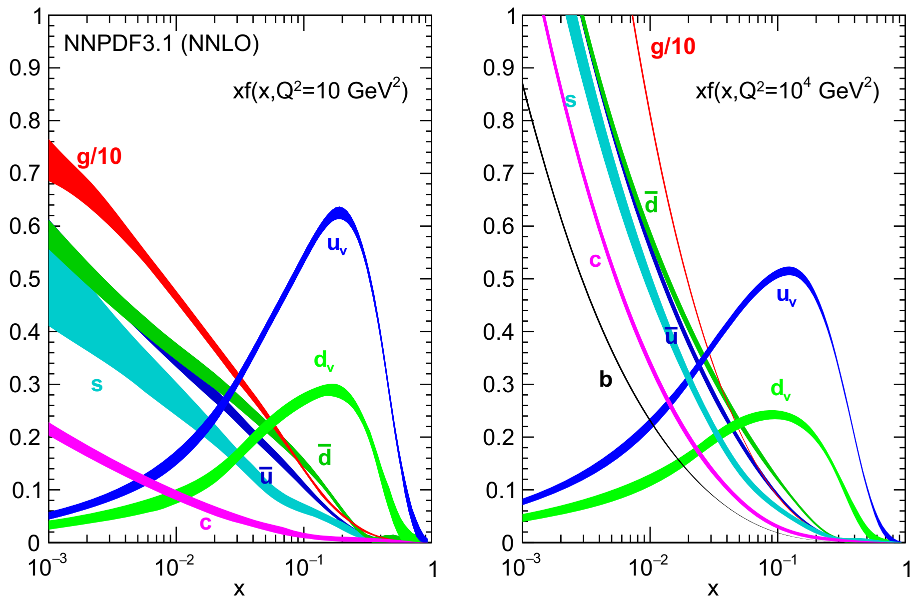

Figure 2.5: Plot of the proton PDF $f_p(x, Q^2)$ times the momentum fraction x as calculated by NNPDF3.1 at NNLO accuracy in perturbation theory for $Q^2 = 10\,\mathrm{GeV}^2$ (left) and $Q^2 = 10^4\,\mathrm{GeV}^2$ (right). Adapted from [24].

3 Beyond the Standard Model

The SM of particle physics is successful. Fine-structure constant $\alpha = e^2/4\pi$ has been precisely calculated and measured [27–30]. In 2012, the discovery of the Higgs boson was announced by the ATLAS and CMS experiments at the CERN LHC [1–3, 11], more than 47 years after its prediction [4, 5]. But there are both problems. The following section highlights several examples of open questions in physics.

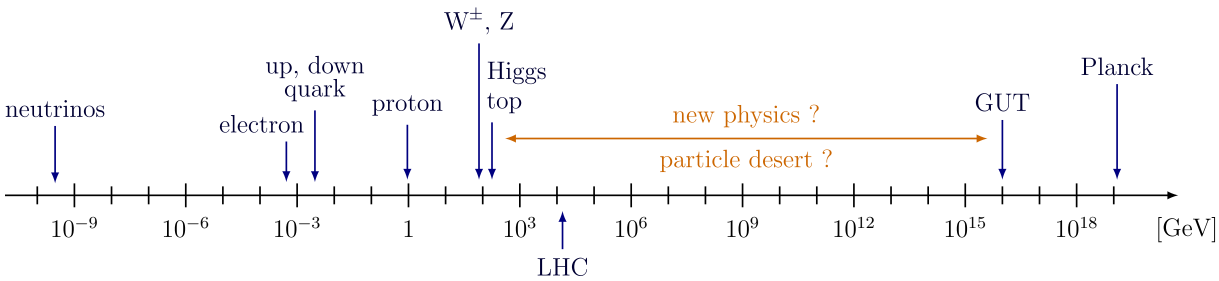

Figure 3.1: Logarithmic scale of different energy scales in particle physics. Adapted from Ref. [9].

4 The CMS Experiment

This chapter will discuss the experimental setup.

4.1 The Large Hadron Collider

The Large Hadron Collider (LHC) is the world's largest and most powerful particle collider with a 27 km circumference and a record collision energy of 13.6 TeV. It surpasses the Tevatron accelerator at Fermilab in the United States [32] (6.3 km, 1.96 TeV), and LEP (209 GeV) [10, Section 32].

During the data-taking period of 2015 to 2018, referred to as "Run 2", the energy of each proton beam was 6.5 TeV, which means the center-of-mass energy was $\sqrt{s} = 13\,\text{TeV}$. The LHC machine is described in more technical detail in Ref. [33].

4.1.1 Luminosity

It depends on several beam parameters. The simplified expression is [10, p. 533]:

$$\mathcal{L} = \frac{N_1 N_2 f}{A}. \tag{4.1}$$

The LHC is designed to reach the nominal luminosity of $\mathcal{L} = 10^{34}\,\text{cm}^{-2}\,\text{s}^{-1}$. See Fig. 4.2. Each bunch contains about 110 billion protons [33, 35].

Figure 4.4 shows the distribution of the number of interactions per bunch crossing in all

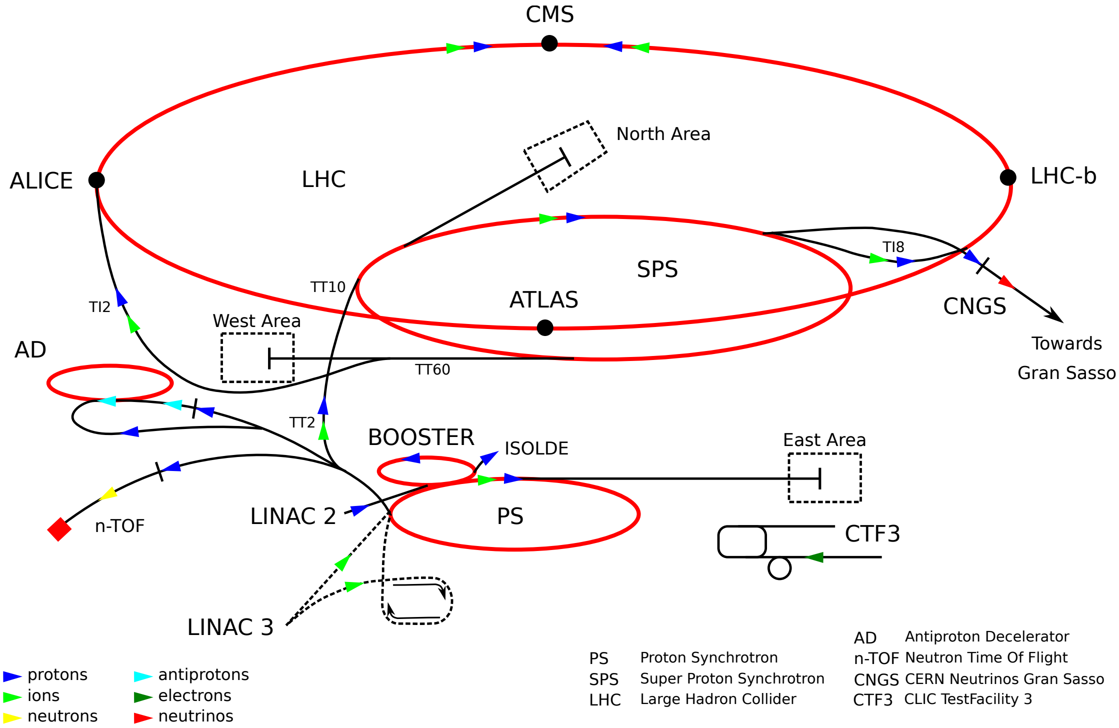

Figure 4.1: CERN's accelerator complex. Taken from [31].

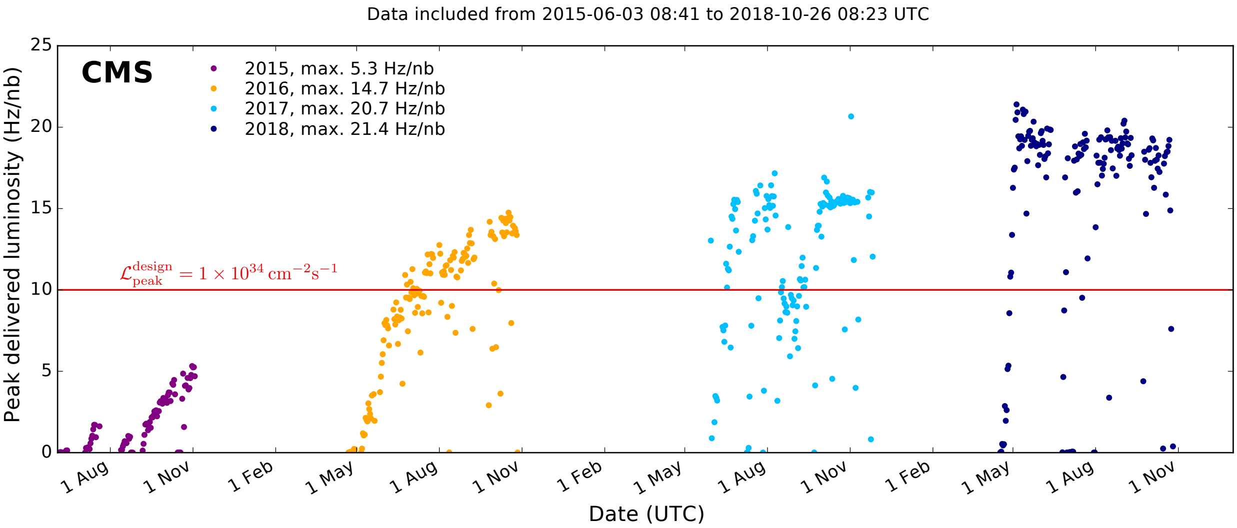

Figure 4.2: The instantaneous luminosity $\mathcal{L}$. The design luminosity is $\mathcal{L}_{\text{peak}}^{\text{design}} = 10^{34}\,\text{cm}^{-2}\,\text{s}^{-1}$. Adapted from [34].

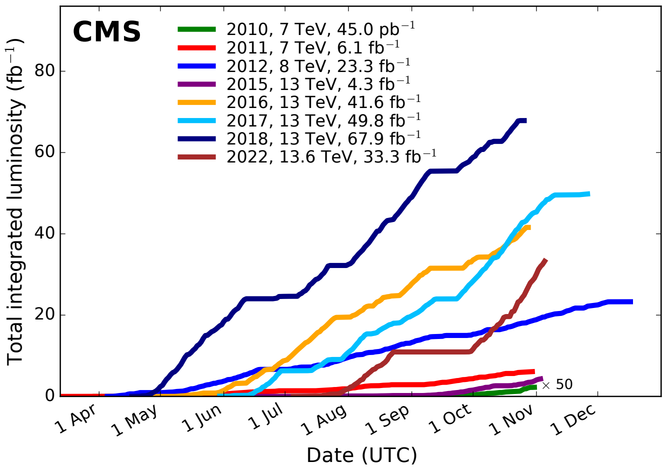

Figure 4.3: Integrated luminosity collected by CMS at $\sqrt{s} = 13\,\text{TeV}$. Figure taken from [34].

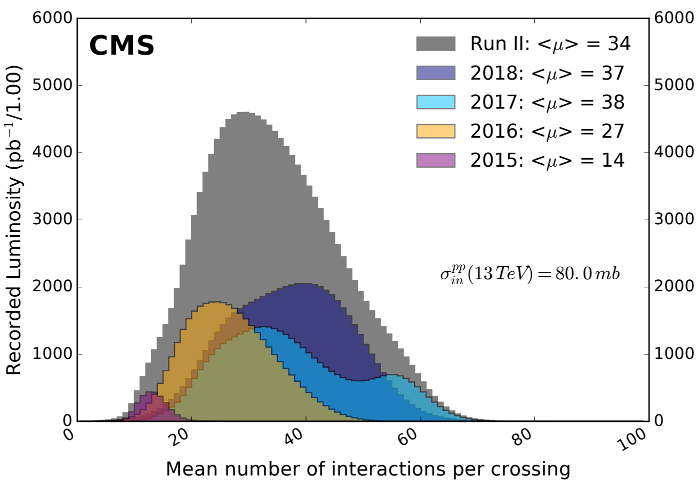

Figure 4.4: Distribution of number of pp interactions, assuming an inelastic cross section of 80 mb. Figure taken from [34].

data-taking years of Run 2.

Figure 4.3 shows a the data of each data-taking year with *integrated luminosity* L, which is

$$L := \int_{\text{data taking}} \mathcal{L}(t)\mathrm{d}t, \tag{4.2}$$

given in units of inverse area, such as the inverse barn (b^{-1}). Between 2016 and 2018, CMS collected about $138\,\mathrm{fb}^{-1}$ of pp collision data for physics analysis.

4.2 The CMS detector

The Compact Muon Solenoid (CMS) detector at one of the interaction points at the LHC. An illustration is shown in Fig. 4.5. A detailed description can be found in Ref. [36].

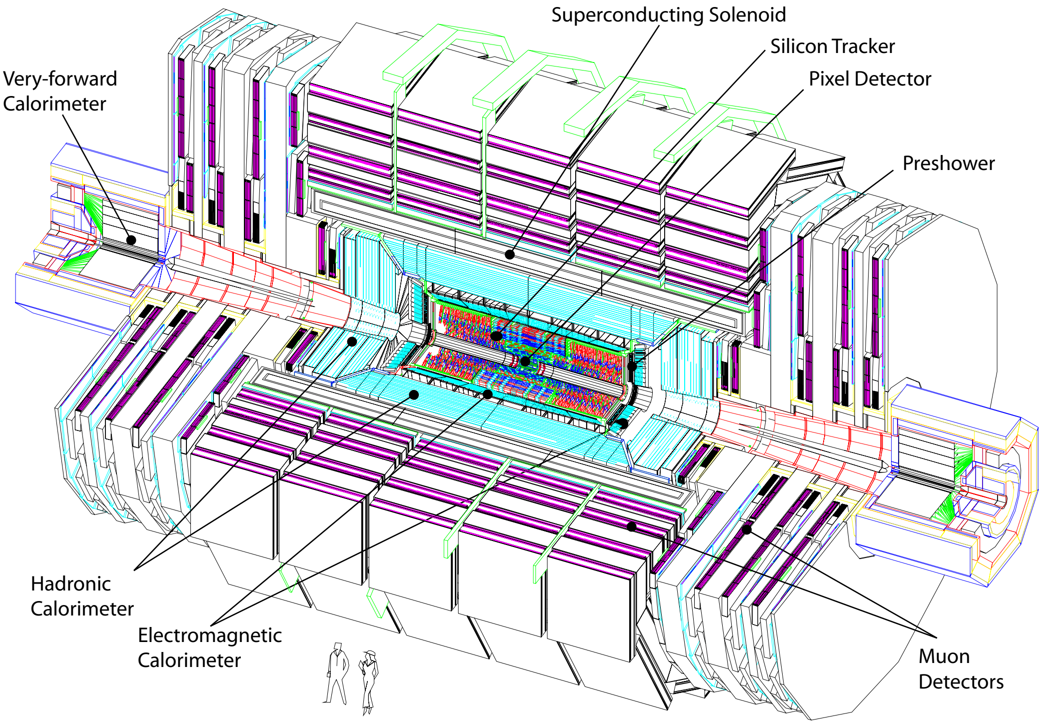

Figure 4.5: The CMS detector. Taken from [36].

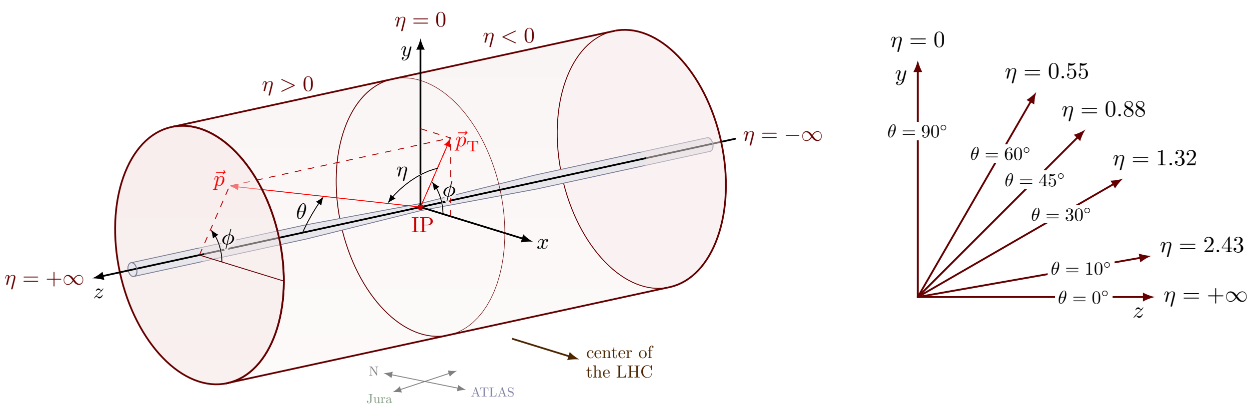

Figure 4.6: Left: The conventional coordinate system of CMS with momentum vector $\vec{p}$. Taken from [37]. **Right**: Pseudorapidity. Taken from [38].

4.2.1 Coordinate system

The conventional coordinate system of CMS is defined in Fig. 4.6.

4.2.2 The solenoid magnet & flux-return yoke

The*superconducting solenoid magnet* is a 13 m long cylinder with an inner diameter of 6 m. The yoke [42].

4.2.3 The pixel tracker

The inner tracker system has a *silicon pixel tracker* and a *silicon microstrip tracker*. Figure 4.8 presents a closer look of the full tracker layout. The pixel tracker from 2008 up to 2016 was composed of 1440 sensor modules with a total of 66 million silicon pixels [43]. During the technical shutdown it was upgraded with 1856 modules with 124 million pixels in total [41, 44]. Their layouts are compared in Fig. 4.9. See Refs. [43, 45] for more information on the resolution.

4.2.4 The silicon strip tracker

The silicon strip tracker is larger. A detailed description of the tracking and vertexing software is given in Ref. [43].

4.2.5 The electromagnetic calorimeter

The *electromagnetic calorimeter* (ECAL) is built around the tracker. The energy resolution can be parametrized as a function of energy [36]:

$$\left(\frac{\sigma_E}{E}\right)^2 = \left(\frac{S}{\sqrt{E}}\right)^2 \oplus \left(\frac{N}{E}\right)^2 \oplus C^2, \tag{4.3}$$

with the stochastic term S, the noise N, and a constant term C. The technical design report [46] describes the ECAL in more technical detail.

4.2.6 The hadronic calorimeter

The last subdetector inside the solenoid is the *hadron calorimeter* (HCAL). The jet energy resolution can be found in Ref. [47]

The *very forward HCAL* (HF) is positioned around the beamline outside the detector.

4.2.7 The muon system

The muon system is outside the solenoid magnet. The final momentum resolution can be roughly parametrized as follows:

$$\left(\frac{\sigma_{p_\mathrm{T}}}{p_\mathrm{T}}\right)^2 = (A \cdot p_\mathrm{T})^2 \oplus C^2, \tag{4.4}$$

where A, and C are constants determined by the hit resolution and multiple scattering, respectively [48]. The resolution grows with momentum, because the track becomes more straight, which increases the uncertainty in its curvature. The technical design report can be found in Ref. [49].

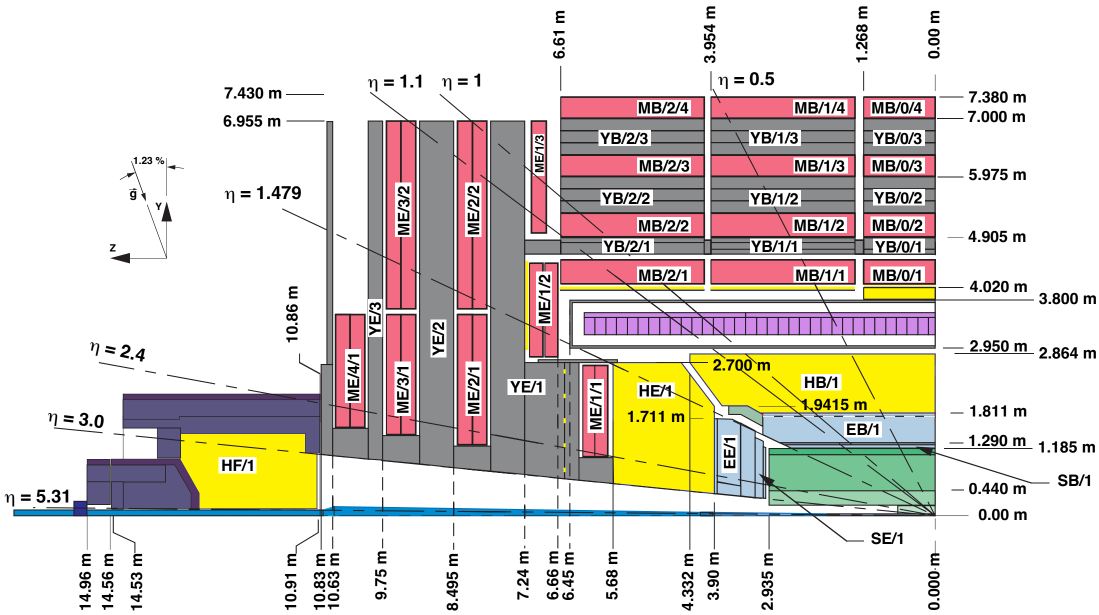

Figure 4.7: Schematic of one quadrant of the CMS detector in the positive zy-plane. Adapted from [39].

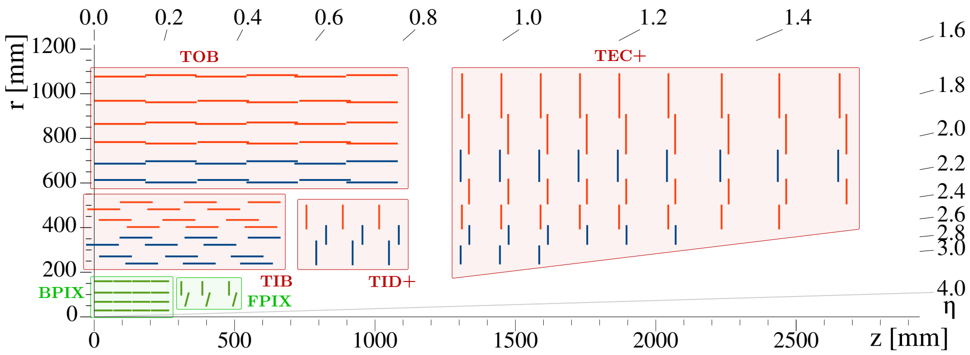

Figure 4.8: Schematic view the CMS tracking system. Adapted from from [40].

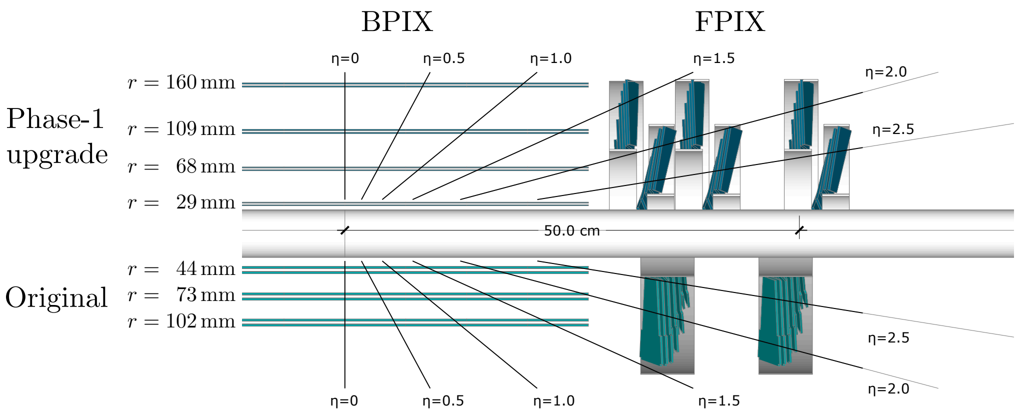

Figure 4.9: Layout of the CMS pixel detector. Adapted from from [41].

4.2.8 The trigger system

The collision rate of 40 MHz is higher than is possible to record offline. The *L1 trigger* has a rate of about 100 kHz. The next level, is the *high-level trigger* (HLT). See Ref. [50].

5 Object & Event Reconstruction

This chapter explains object and event reconstruction in the CMS experiment.

5.1 Principles of particle identification

Figure 5.1 compares the lifetime, dividing them in different regions of stability in the context of the CMS experiment.

Each of these particles has a unique set of properties that leave a characteristic signal in one or more of the subdetector, as illustrated in Fig. 5.2.

5.2 Particle-flow algorithm

The particle-flow (PF) algorithm [53, 54] fully reconstructs the event of a pp collision with an optimized combination of all measurements of the CMS subsystems.

Tracks in the inner tracker or muon system are iteratively built from hits, using the *Kalman-filter* (KF) *technique* [55, 56].

5.3 Primary vertex

The algorithm locates primary vertices (PVs) of pp collisions. The tracks are clustered using the *deterministic annealing algorithm* [57]. Finally, candidate vertices are fitted using an *adaptive vertex fitter* [58]. The PV with the largest sum of momenta is assumed to be the vertex of the hard scattering process [43, 54, 59].

5.4 Electrons

Electrons are reconstructed by associating a track in the inner tracker to clusters of energy deposits in the ECAL. Candidate tracks are refitted with the *Gaussian sum filter* (GSF) [60]. The ECAL clusters are recombined into a so-called *supercluster*. The resolution is documented in Ref. [61, 62].

The reconstruction and identification of electrons, as well as high-energy photons, are discussed in more detail in Refs. [63] and [61].

The *relative isolation* for electrons is computed with the so-called *rho-effective-area method* [64]:

$$I_{\mathrm{rel}}^{\mathrm{e}} := \frac{\sum_{\mathrm{charged}} p_{\mathrm{T}} + \max\left(0, \sum_{\mathrm{neutral}} E_{\mathrm{T}} - \rho A_{\mathrm{eff}}\right)}{p_{\mathrm{T}}^{\mathrm{e}}}. \tag{5.1}$$

5.5 Muons

Muon candidates in CMS are reconstructed as *standalone muons*, *tracker muons*, and/or *global muons* [65].

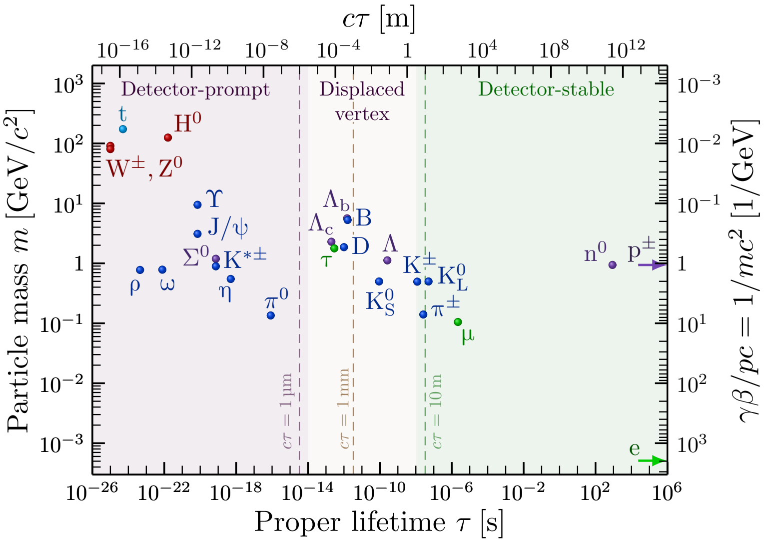

Figure 5.1: Plot of the mass versus lifetime τ of many composite and fundamental SM particles. The decay length is given by $L = \gamma\beta c\tau$, with $\gamma\beta = p/mc$. Adapted from [51].

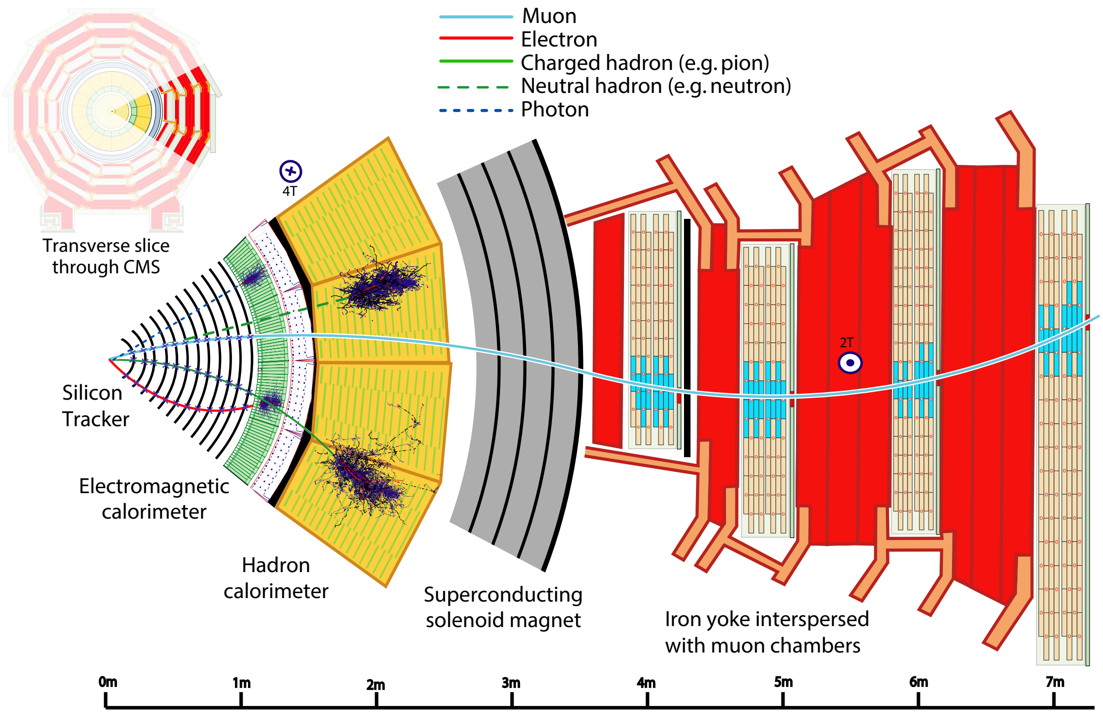

Figure 5.2: Particles in the CMS detector. Adapted from from [52].

The relative isolation of a muon is defined with the so-called $\Delta\beta$*-corrections*:

$$I^{\mu}_{\mathrm{rel}} := \frac{\sum_{\mathrm{charged}} p_{\mathrm{T}} + \max\left(0, \sum_{\mathrm{neutral}} E_{\mathrm{T}} - \Delta\beta \sum_{\mathrm{charged,\ PU}} p_{\mathrm{T}}\right)}{p^{\mu}_{\mathrm{T}}}. \tag{5.2}$$

5.6 Hadronically Decayed τ Leptons

Hadronic decays of τ leptons (τ_{h}) are reconstructed with the *hadron-plus-strips* (HPS) *algorithm* [66–69]. About 65% of hadronic τ decays involve neutral pions, which decay promptly ($\tau = 8.4 \times 10^{-17}$ s) to two photons 98.8% of the time [10, p. 33].

The τ_{h} identification algorithm DeepTau [69] was used to discriminate against jets that are initiated by quarks and gluons, as well as electrons and muons, see Fig. 5.5.

5.7 Jets

Jets are reconstructed with a clustering algorithm. The jet properties must be *infrared safe* and *collinear safe*. The *anti-*k_T (AK) *algorithm* utilizes the metric

$$d_{ij} = \min\left(p^{-2}_{\mathrm{T,i}}, p^{-2}_{\mathrm{T,j}}\right) \frac{\Delta R^2_{ij}}{\Delta R^2_y}, \tag{5.3}$$

where $\Delta R_y = \sqrt{\Delta y^2 + \Delta\phi^2}$ is the distance in (y, ϕ)-space with the *rapidity*

$$y := \frac{1}{2} \ln\left(\frac{E + p_z}{E - p_z}\right). \tag{5.4}$$

If a cluster i of combined objects satisfies

$$d_{ij} > d_{i\mathrm{B}} = p^{-2}_{\mathrm{T,i}}, \tag{5.5}$$

More info is given in Ref. [54, 71]. The AK algorithm is implemented in the FastJet library [72, 73], and *charged-hadron subtraction* (CHS) is used.

The CMS Collaboration determines *jet energy corrections* (JECs) in several steps, which are explained in detail in Ref. [74]. Additionally, the jet energy and *jet energy resolution* (JER) of jets in simulation are corrected to obtain better agreement between simulation and data.

Genuine jets are distinguished from pileup jets with the identification algorithm [75]. Identification [76] removes spurious jet-like features that originate from isolated noise patterns in certain HCAL regions.

5.8 Bottom quark identification

The DeepCSV algorithm [77, 78] for b tagging jets. DeepCSV is a deep neural network (DNN) with four hidden layers that is an extension of the combined secondary vertex (CSV) algorithm [77, 78].

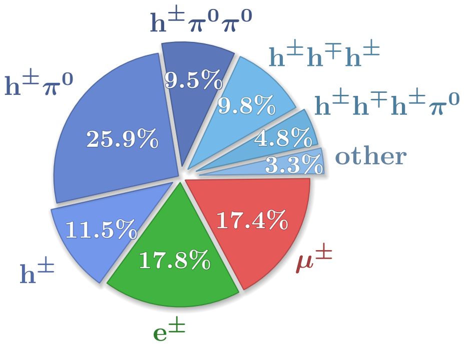

Figure 5.3: Pie charts of branching fractions. **Left**: τ lepton decay. **Right**: Decay channels of a pair of τ leptons. Numbers from PDG [10, p. 28].

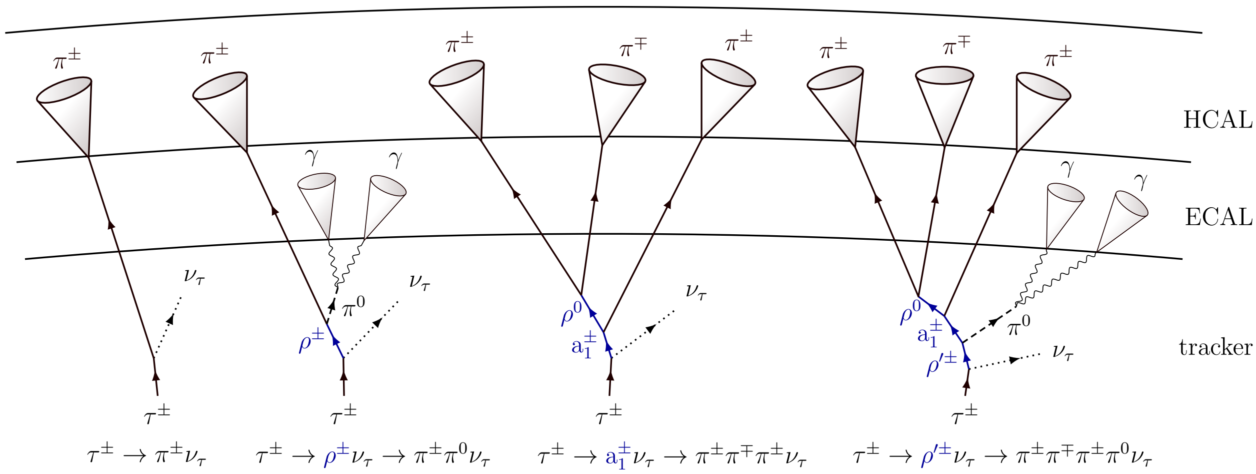

Figure 5.4: An illustration τ_h signatures. Inspired by Ref. [70, p. 37].

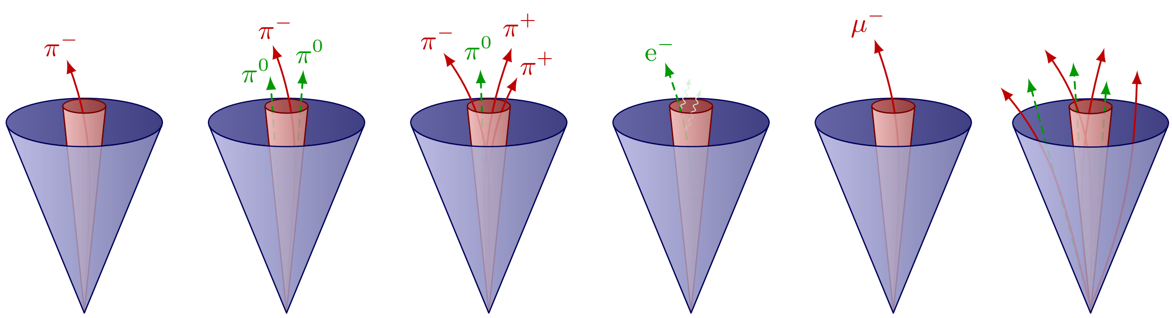

(a) Genuine π^-. **(b)** Genuine $\pi^-\pi^0\pi^0$. **(c)** Genuine $\pi^+\pi^-\pi^+\pi^0$. **(d)** Isolated electron. **(e)** Isolated muon. **(f)** Quark or gluon jet.

Figure 5.5: Illustration of several hadronic decay modes of the τ leptons (a-c) and their backgrounds (d-f).

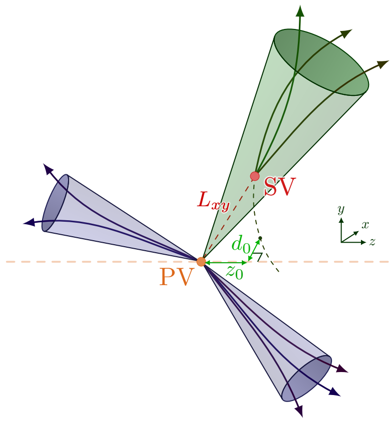

Figure 5.6: B-tagging.

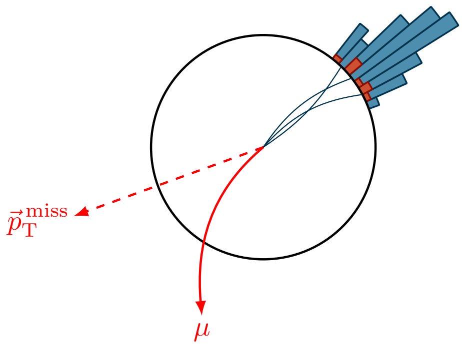

Figure 5.7: Illustration of missing transverse energy (MET) with a muon track (red), and energy deposits in the calorimeters.

5.9 Missing transverse energy

The vectorially sum of all particles gives the missing momentum

$$\vec{p}_{\mathrm{T}}^{\mathrm{miss}} = -\sum_{\mathrm{i}} \vec{p}_{\mathrm{T}}^{\,i}. \tag{5.6}$$

This vector, or its length, is often referred to as the *missing transverse momentum*, or *missing transverse energy* (MET). Several corrections are applied [54]. More details can be found in Refs. [79] and [80].

6 Data sets & Simulated Samples

This chapter will discuss in more detail the data sets of pp collision events used, as well as the samples of simulated background events.

6.1 Data sets

The total data set recorded between 2016 and 2018 corresponds to an integrated luminosity of approximately $138\,\mathrm{fb}^{-1}$ at $\sqrt{s} = 13\,\mathrm{TeV}$. The run ranges and integrated luminosity per year are listed in Table 6.1.

Table 6.1: LHC run number ranges and integrated luminosity L.

Run number range	L [fb^{-1}]
272007–284044	36.3
297020–306462	41.5
315252–325175	59.7

6.2 Event simulation

The PYTHIA parameters affecting the description of the underlying event are set to the CUETP8M1 (CP5) tune for all 2016 (2017 and 2018) samples [82, 83], except for the 2016 $\mathrm{t\bar{t}}$ sample, for which CUETP8M2T4 [84] is used. The interaction with the CMS detector is simulated by GEANT4 [85]. Pileup is generated with PYTHIA. Event generation is described in more detail in Refs. [10, p. 717], [86] and [87].

6.3 Backgrounds

6.3.1 Simulated backgrounds

All the simulated background samples used in this thesis are listed in Table 6.2. The W + jets and Z + jets processes are generated with MADGRAPH [88] at LO precision. The MLM jet matching and merging scheme [89] is used to match partons between MADGRAPH and PYTHIA and prevent overcounting. The Z + jets samples generated at NLO by MADGRAPH5_aMC@NLO [90]. The production of $\mathrm{t\bar{t}}$ and singly produced top quarks is simulated with the POWHEG [91–93] 2.0 and 1.0 generators, respectively, at NLO precision [94–97]. Diboson production is generated at LO with PYTHIA 8 [98, 99]. The NNPDF3.0 PDF sets [100] are used for 2016. The NNPDF3.1 PDF [24] sets are used for 2017 and 2018 samples.

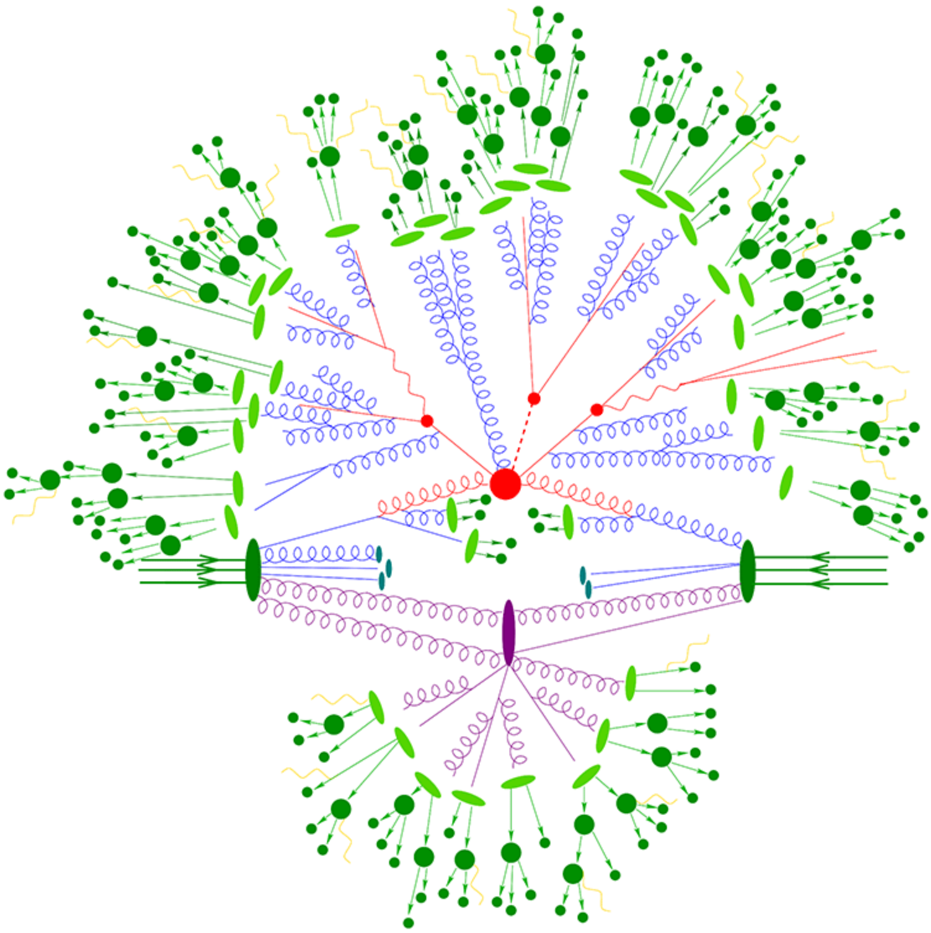

Figure 6.1: Schematic diagram explaining event generation of two colliding protons. Retrieved from [81].

Table 6.2: Summary of simulated SM backgrounds

Process	Generators	Cross section σ [pb]
Drell-Yan, $\mathbf{Z/\gamma^* \to \ell^+\ell^-}$, LO		
$+$jets, $10 < m_{\ell\ell} < 50\,\text{GeV}$	MadGraph, pythia	15810.0 (LO), 18610.0 (NLO)
$+$jets, $m_{\ell\ell} > 50\,\text{GeV}$	MadGraph, pythia	5343.0 (LO), 6077.2 (NNLO)
$+\,1$ jets, $m_{\ell\ell} > 50\,\text{GeV}$	MadGraph, pythia	877.8 (LO)
$+\,2$ jets, $m_{\ell\ell} > 50\,\text{GeV}$	MadGraph, pythia	304.4 (LO)
$+\,3$ jets, $m_{\ell\ell} > 50\,\text{GeV}$	MadGraph, pythia	111.5 (LO)
$+\,4$ jets, $m_{\ell\ell} > 50\,\text{GeV}$	MadGraph, pythia	44.05 (LO)
Drell-Yan, $\mathbf{Z/\gamma^* \to \ell^+\ell^-}$, NLO		
$+$jets, $m_{\ell\ell} \in [100, 200[\,\text{GeV}$	aMC@NLO, pythia	247.8 (NLO)
$+$jets, $m_{\ell\ell} \in [200, 400[\,\text{GeV}$	aMC@NLO, pythia	8.502 (NLO)
$+$jets, $m_{\ell\ell} \in [400, 500[\,\text{GeV}$	aMC@NLO, pythia	0.4514 (NLO)
$+$jets, $m_{\ell\ell} \in [500, 700[\,\text{GeV}$	aMC@NLO, pythia	0.2558 (NLO)
$+$jets, $m_{\ell\ell} \in [700, 800[\,\text{GeV}$	aMC@NLO, pythia	0.04023 (NLO)
$+$jets, $m_{\ell\ell} \in [800, 1000[\,\text{GeV}$	aMC@NLO, pythia	0.03406 (NLO)
$+$jets, $m_{\ell\ell} \in [1000, 1500[\,\text{GeV}$	aMC@NLO, pythia	0.01828 (NLO)
$+$jets, $m_{\ell\ell} \in [1500, 2000[\,\text{GeV}$	aMC@NLO, pythia	0.002367 (NLO)
$+$jets, $m_{\ell\ell} \in [2000, 3000[\,\text{GeV}$	aMC@NLO, pythia	5.409×10^{-4} (NLO)
$+$jets, $m_{\ell\ell} \in [3000, \infty[\,\text{GeV}$	aMC@NLO, pythia	3.048×10^{-5} (NLO)
$\mathbf{W + jets, W \to \ell\nu}$		
$+$jets	MadGraph, pythia	52940.0 (LO), 61526.7 (NLO)
$+\,1$ jets	MadGraph, pythia	8104.0 (LO)
$+\,2$ jets	MadGraph, pythia	2793.0 (LO)
$+\,3$ jets	MadGraph, pythia	992.5 (LO)
$+\,4$ jets	MadGraph, pythia	544.3 (LO)
$\mathbf{t\bar{t} + jets}$		833.9 (NNLO)
Fully leptonic	powheg, pythia	88.29 (NNLO), $\mathcal{B} = 10.6\%$
Semi-leptonic	powheg, pythia	365.35 (NNLO), $\mathcal{B} = 43.9\%$
Fully Hadronic	powheg, pythia	377.96 (NNLO), $\mathcal{B} = 45.4\%$
Single top		
$\mathrm{t} + \mathrm{W}^-$	powheg, pythia	35.85 (NNLO)
$\bar{\mathrm{t}} + \mathrm{W}^+$	powheg, pythia	35.85 (NNLO)
Single t, t channel	powheg, pythia	136.02 (NNLO)
Single $\bar{\mathrm{t}}$, t channel	powheg, pythia	80.95 (NNLO)
Diboson		
WW	pythia	75.88 (LO)
WZ	pythia	27.60 (LO)
ZZ	pythia	12.14 (LO)

6.3.2 Cross sections

Table 6.2 also lists the theoretical cross sections σ for each sample. The events are weighted by

$$Z = \frac{L\sigma}{N_{\mathrm{tot}}}, \tag{6.1}$$

or with generator weight w_{gen},

$$Z = \frac{L\sigma}{\sum w_{\mathrm{gen}}} w_{\mathrm{gen}}. \tag{6.2}$$

The LO cross sections of the $\mathrm{Z}+\mathrm{jets}$ and $\mathrm{W}+\mathrm{jets}$ samples in Table 6.2 are computed with MadGraph. The $\mathrm{Z}+\mathrm{jets}$ cross section is computed with fewz [101] program at NNLO in perturbative QCD, and with NLO electroweak corrections. The $\mathrm{t\bar{t}}$+jets cross section was computed with the Top++v2.0 program [102, 103] at NNLO and at next-to-next-to-leading logarithmic (NNLL) accuracy. The $\mathrm{W}+\mathrm{jets}$ production is normalized with cross sections computed at NLO accuracy.

7 Event Selection

This chapter will discuss in more detail the data sets of pp collision events used, as well as the samples of simulated background events.

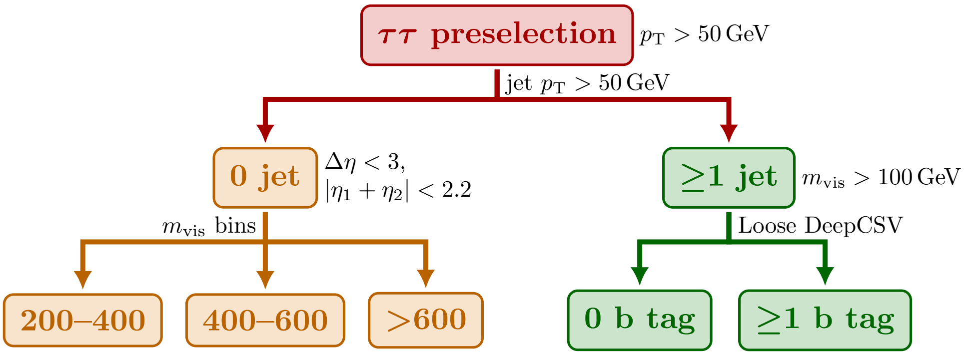

Figure 7.1: Flow chart of event selection.

References

[1] **CMS** Collaboration, "Observation of a new boson at a mass of 125 GeV with the CMS experiment at the LHC", *Phys. Lett. B* **716** (2012) 30, doi:10.1016/j.physletb.2012.08.021, arXiv:1207.7235.

[2] **ATLAS** Collaboration, "Observation of a new particle in the search for the Standard Model Higgs boson with the ATLAS detector at the LHC", *Phys. Lett. B* **716** (2012) 1, doi:10.1016/j.physletb.2012.08.020, arXiv:1207.7214.

[3] **CMS** Collaboration, "Observation of a new boson with mass near 125 GeV in pp collisions at $\sqrt{s} = 7$ and 8 TeV", *JHEP* **06** (2013) 081, doi:10.1007/JHEP06(2013)081, arXiv:1303.4571.

[4] F. Englert and R. Brout, "Broken Symmetry and the Mass of Gauge Vector Mesons", *Phys. Rev. Lett.* **13** (1964) 321, doi:10.1103/PhysRevLett.13.321.

[5] P. W. Higgs, "Broken Symmetries and the Masses of Gauge Bosons", *Phys. Rev. Lett.* **13** (1964) 508, doi:10.1103/PhysRevLett.13.508.

[6] L. M. Brown, M. Dresden, L. H. Hoddeson, and M. West, eds., "Proceedings, 2nd International Symposium on on the History of Particle Physics in the 1950s: Pions to Quarks: Batavia, USA, May 1-4, 1985". Univ. Pr., Cambridge, UK, (1989).

[7] L. H. Hoddeson, L. Brown, M. Riordan, and M. Dresden, eds., "The Rise of the standard model: Particle physics in the 1960s and 1970s. Proceedings, Conference, Stanford, USA, June 24-27, 1992". (1997).

[8] D. Griffiths, "Introduction to Elementary Particles". Wiley-VCH, 2 edition, 2008. ISBN 978-3-527-40601-2.

[9] Neutelings, Izaak, "History timeline and energy scales – TikZ.net", https://tikz.net/timeline/, 2022. (Retrieved March 26, 2022).

[10] **Particle Data** Group, "Review of Particle Physics", *PTEP* **2022** (2022) 083C01, doi:10.1093/ptep/ptac097.

[11] **ATLAS** and **CMS** Collaborations, "Combined Measurement of the Higgs Boson Mass in pp Collisions at $\sqrt{s} = 7$ and 8 TeV with the ATLAS and CMS Experiments", *Phys. Rev. Lett.* **114** (2015) 114, doi:10.1103/PhysRevLett.114.191803, arXiv:1503.07589.

[12] A. Ferrari and N. Rompotis, "Exploration of Extended Higgs Sectors with Run-2 Proton–Proton Collision Data at the LHC", *Symmetry* **13** (2021), no. 11, 2144, doi:10.3390/sym14081546. [Erratum: Symmetry 14, 1546 (2022)].

[13] Wikimedia Commons, "File:Standard Model of Elementary Particles.svg — Wikimedia Commons, the free media repository", https://commons.wikimedia.org/wiki/File:Standard_Model_of_Elementary_Particles.svg, 2023. (Retrieved Jan 13, 2023).

[14] G. Isidori, "Lectures notes on Flavour physics",

https://www.physik.uzh.ch/en/groups/isidori/teaching.html, 2016. (Retrieved Nov 16, 2022).

[15] S. L. Glashow, J. Iliopoulos, and L. Maiani, "Weak Interactions with Lepton-Hadron Symmetry", *Phys. Rev. D* **2** (1970) 1285, doi:10.1103/PhysRevD.2.1285.

[16] E. D. Bloom et al., "High-Energy Inelastic e^{-}p Scattering at 6° and 10°", *Phys. Rev. Lett.* **23** (1969) 930, doi:10.1103/PhysRevLett.23.930.

[17] M. Breidenbach et al., "Observed Behavior of Highly Inelastic Electron-Proton Scattering", *Phys. Rev. Lett.* **23** (1969) 935, doi:10.1103/PhysRevLett.23.935.

[18] **ZEUS** and **H1** Collaborations, "Combination of measurements of inclusive deep inelastic $e^{\pm}$p scattering cross sections and QCD analysis of HERA data", *Eur. Phys. J. C* **75** (2015), no. 12, 580, doi:10.1140/epjc/s10052-015-3710-4, arXiv:1506.06042.

[19] R. P. Feynman, "The Behavior of Hadron Collisions at Extreme Energies", in *High Energy Collisions: Third International Conference*, p. 237. Stony Brook, N.Y., U.S.A., 1969.

[20] J. D. Bjorken and E. A. Paschos, "Inelastic Electron-Proton and γ-Proton Scattering and the Structure of the Nucleon", *Phys. Rev.* **185** (1969) 1975, doi:10.1103/PhysRev.185.1975.

[21] J. M. Campbell, J. W. Huston, and W. J. Stirling, "Hard Interactions of Quarks and Gluons: A Primer for LHC Physics", *Rept. Prog. Phys.* **70** (2007) 89, doi:10.1088/0034-4885/70/1/R02, arXiv:hep-ph/0611148.

[22] R. Placakyte, "Parton Distribution Functions", in *Proceedings, 31st International Conference on Physics in collisions (PIC 2011).* Vancouver, Canada, 2011. arXiv:1111.5452.

[23] **ALICE** Collaboration, "Parton distributions for the LHC", *Eur. Phys. J. C* **63** (2009) 189, doi:10.1140/epjc/s10052-009-1072-5, arXiv:0901.0002.

[24] **NNPDF** Collaboration, "Parton distributions from high-precision collider data", *Eur. Phys. J. C* **77** (2017), no. 10, 663, doi:10.1140/epjc/s10052-017-5199-5, arXiv:1706.00428.

[25] J. C. Collins and D. E. Soper, "The Theorems of Perturbative QCD", *Ann. Rev. Nucl. Part. Sci.* **37** (1987) 383, doi:10.1146/annurev.ns.37.120187.002123.

[26] J. C. Collins, D. E. Soper, and G. F. Sterman, "Factorization of Hard Processes in QCD", *Adv. Ser. Direct. High Energy Phys.* **5** (1989) 11, doi:10.1142/9789814503266_0001, arXiv:hep-ph/0409313.

[27] T. Aoyama, M. Hayakawa, T. Kinoshita, and M. Nio, "Tenth-Order QED Contribution to the Electron g-2 and an Improved Value of the Fine Structure Constant", *Phys. Rev. Lett.* **109** (2012) 111807, doi:10.1103/PhysRevLett.109.111807, arXiv:1205.5368.

[28] T. Aoyama, M. Hayakawa, T. Kinoshita, and M. Nio, "Tenth-Order Electron Anomalous Magnetic Moment — Contribution of Diagrams without Closed Lepton Loops", *Phys. Rev. D* **91** (2015), no. 3, 033006, doi:10.1103/PhysRevD.91.033006,10.1103/PhysRevD.96.019901, arXiv:1412.8284. [Erratum: Phys. Rev. D96, no.1, 019901 (2017)].

[29] M. Nio, “QED tenth-order contribution to the electron anomalous magnetic moment and a new value of the fine-structure constant”, Fundamental Constants Meeting, Eltville, Germany, 2015. http://www.bipm.org/cc/CODATA-TGFC/Allowed/2015-02/Nio.pdf.

[30] D. Hanneke, S. Fogwell, and G. Gabrielse, “New Measurement of the Electron Magnetic Moment and the Fine Structure Constant”, *Phys. Rev. Lett.* **100** (2008) 120801, doi:10.1103/PhysRevLett.100.120801, arXiv:0801.1134.

[31] L. Forthomme (Wikimedia Commons), “File:Cern-accelerator-complex.svg — Wikimedia Commons, the free media repository”, https://commons.wikimedia.org/wiki/File:Cern-accelerator-complex.svg, 2016. (Retrieved Jul 24, 2017).

[32] S. Holmes, R. S. Moore, and V. Shiltsev, “Overview of the Tevatron Collider Complex: Goals, Operations and Performance”, *JINST* **6** (2011) T08001, doi:10.1088/1748-0221/6/08/T08001, arXiv:1106.0909.

[33] L. Evans and P. Bryant, “LHC Machine”, *JINST* **3** (2008), no. 08, S08001, doi:10.1088/1748-0221/3/08/S08001.

[34] **CMS** Collaboration, “Public CMS Luminosity Information”. https://twiki.cern.ch/twiki/bin/view/CMSPublic/LumiPublicResults. (Retrieved Dec 6, 2022).

[35] I. Efthymiopoulos et al., “Bunch Luminosity Variations in LHC Run 2. BUNCH LUMINOSITY VARIATIONS IN LHC RUN 2”, *JACoW IPAC* **2021** (2021) 4094, doi:10.18429/JACoW-IPAC2021-THPAB172.

[36] **CMS** Collaboration, “The CMS experiment at the CERN LHC”, *JINST* **3** (2008) S08004, doi:10.1088/1748-0221/3/08/S08004.

[37] Neutelings, Izaak, “CMS coordinate system – TikZ.net”, https://tikz.net/axis3d_cms/, 2022. (Retrieved Dec 2, 2022).

[38] Neutelings, Izaak, “Pseudorapidity – TikZ.net”, https://tikz.net/axis2d_pseudorapidity/, 2022. (Retrieved Dec 2, 2022).

[39] **CMS** Collaboration, “Performance of the CMS Drift Tube Chambers with Cosmic Rays”, *JINST* **5** (2010) T03015, doi:10.1088/1748-0221/5/03/T03015, arXiv:0911.4855.

[40] **CMS** Collaboration, “CMS Tracker Detector Performance Results”, https://twiki.cern.ch/twiki/bin/view/CMSPublic/DPGResultsTRK, 2022. (Retrieved Dec 2, 2022).

[41] **CMS Tracker** Group, “The CMS Phase-1 Pixel Detector Upgrade”, *JINST* **16** (2021), no. 02, P02027, doi:10.1088/1748-0221/16/02/P02027, arXiv:2012.14304.

[42] **CMS** Collaboration, “Precise Mapping of the Magnetic Field in the CMS Barrel Yoke using Cosmic Rays”, *JINST* **5** (2015) T03021, doi:10.1088/1748-0221/5/03/T03021, arXiv:0910.5530.

[43] **CMS** Collaboration, “Description and performance of track and primary-vertex reconstruction with the CMS tracker”, *JINST* **9** (2014) P10009, doi:10.1088/1748-0221/9/10/P10009, arXiv:1405.6569.

[44] **CMS** Collaboration, "The Phase-1 upgrade of the CMS pixel detector", *JINST* **12** (2017), no. 07, C07009, doi:10.1088/1748-0221/12/07/C07009.

[45] **CMS** Collaboration, "CMS Tracking POG Performance Plots For 2017 with PhaseI pixel detector", https://twiki.cern.ch/twiki/bin/view/CMSPublic/TrackingPOGPerformance2017MC#Vertex_Resolutions, 2022. (Retrieved Dec 8, 2022).

[46] **CMS** Collaboration, "The CMS electromagnetic calorimeter project: Technical Design Report", Technical Design Report CMS. CERN, Geneva, 1997.

[47] **CMS** Collaboration, "Jet energy scale and resolution in the CMS experiment in pp collisions at 8 TeV", *JINST* **12** (2017), no. 02, P02014, doi:10.1088/1748-0221/12/02/P02014, arXiv:1607.03663.

[48] E. Manca, "Validation of the muon momentum resolution in view of the W mass measurement with the CMS experiment". PhD thesis, INFN, Pisa, 2016. CMS-TS-2016-024, CERN-THESIS-2016-173.

[49] **CMS** Collaboration, "The CMS muon project : Technical Design Report", Technical Design Report CMS. CERN, Geneva, 1997.

[50] **CMS** Collaboration, "The CMS trigger system", *JINST* **12** (2017) P01020, doi:10.1088/1748-0221/12/01/P01020, arXiv:1609.02366.

[51] L. Lee, C. Ohm, A. Soffer, and T.-T. Yu, "Collider Searches for Long-Lived Particles Beyond the Standard Model", *Prog. Part. Nucl. Phys.* **106** (2019) 210, doi:10.1016/j.ppnp.2019.02.006, arXiv:1810.12602. [Erratum: Prog.Part.Nucl.Phys. 122, 103912 (2022)].

[52] D. Barney, "CMS Slice", https://cds.cern.ch/record/2628641/, 2015. (Retrieved Dec 8, 2022).

[53] **CMS** Collaboration, "Commissioning of the Particle-flow Event Reconstruction with the first LHC collisions recorded in the CMS detector", CMS Physics Analysis Summary CMS-PAS-PFT-10-001, CERN, 2010.

[54] **CMS** Collaboration, "Particle-flow reconstruction and global event description with the CMS detector", *JINST* **12** (2017) P10003, doi:10.1088/1748-0221/12/10/P10003, arXiv:1706.04965.

[55] W. Adam, B. Mangano, T. Speer, and T. Todorov, "Track Reconstruction in the CMS tracker", technical report, CERN, Geneva, 2006.

[56] R. Fruhwirth, "Application of Kalman filtering to track and vertex fitting", *Nucl. Instrum. Meth. A* **262** (1987) 444, doi:10.1016/0168-9002(87)90887-4.

[57] K. Rose, "Deterministic annealing for clustering, compression, classification, regression, and related optimization problems", *IEEE Proc.* **86** (1998), no. 11, 2210, doi:10.1109/5.726788.

[58] R. Frühwirth, W. Waltenberger, and P. Vanlaer, "Adaptive Vertex Fitting", technical report, CERN, Geneva, 2007.

[59] **CMS** Collaboration, "Technical proposal for the Phase-II upgrade of the Compact Muon Solenoid", CMS Technical Proposal CERN-LHCC-2015-010, CMS-TDR-15-02, CERN,

2015.

[60] W. Adam, R. Frühwirth, A. Strandlie, and T. Todorov, "Reconstruction of electrons with the Gaussian-sum filter in the CMS tracker at the LHC", *Journal of Physics G: Nuclear and Particle Physics* **31** (2005), no. 9, N9, `doi:10.1088/0954-3899/31/9/n01`.

[61] **CMS** Collaboration, "Electron and photon reconstruction and identification with the CMS experiment at the CERN LHC", *JINST* **16** (2021) P05014, `doi:10.1088/1748-0221/16/05/P05014`, `arXiv:2012.06888`.

[62] **CMS** Collaboration, "ECAL 2016 refined calibration and Run2 summary plots", CMS Detector Performance Summary CMS-DP-2020-021, CERN, 2020.

[63] **CMS** Collaboration, "Performance of electron reconstruction and selection with the CMS detector in proton-proton collisions at $\sqrt{s} = 8\,\text{TeV}$", *JINST* **10** (2015) P06005, `doi:10.1088/1748-0221/10/06/P06005`, `arXiv:1502.02701`.

[64] M. Cacciari and G. P. Salam, "Pileup subtraction using jet areas", *Phys. Lett. B* **659** (2008) 119, `doi:10.1016/j.physletb.2007.09.077`, `arXiv:0707.1378`.

[65] **CMS** Collaboration, "Performance of the CMS muon detector and muon reconstruction with proton-proton collisions at $\sqrt{s} =$ 13 TeV", *JINST* **13** (2018) P06015, `doi:10.1088/1748-0221/13/06/P06015`, `arXiv:1804.04528`.

[66] **CMS** Collaboration, "Performance of τ-lepton reconstruction and identification in CMS", *JINST* **7** (2012), no. 01, P01001, `doi:10.1088/1748-0221/7/01/P01001`, `arXiv:1109.6034`.

[67] **CMS** Collaboration, "Performance of reconstruction and identification of τ leptons decaying to hadrons and ν_τ in pp collisions at $\sqrt{s} =$ 13 TeV", *JINST* **13** (2018) P10005, `doi:10.1088/1748-0221/13/10/P10005`, `arXiv:1809.02816`.

[68] **CMS** Collaboration, "Performance of reconstruction and identification of tau leptons in their decays to hadrons and tau neutrino in LHC Run-2", CMS Physics Analysis Summary CMS-PAS-TAU-16-002, CERN, 2016.

[69] **CMS** Collaboration, "Identification of hadronic tau lepton decays using a deep neural network", *JINST* **17** (2022), no. 07, P07023, `doi:10.1088/1748-0221/17/07/p07023`, `arXiv:2201.08458`.

[70] Y. Takahashi and M. Tomoto, "Measurement of the top-quark pair production cross-section in *pp* collisions at $\sqrt{s} = 7\,\text{TeV}$ using final states with an electron or a muon and a hadronically decaying τ-lepton". PhD thesis, Nagoya University, 2012. CERN-THESIS-2012-252.

[71] M. Cacciari, G. P. Salam, and G. Soyez, "The anti-$\mathrm{k_t}$ jet clustering algorithm", *JHEP* **04** (2008) 063, `doi:10.1088/1126-6708/2008/04/063`, `arXiv:0802.1189`.

[72] M. Cacciari and G. P. Salam, "Dispelling the N^3 myth for the k_T jet-finder", *Phys. Lett. B* **641** (2006) 57, `doi:10.1016/j.physletb.2006.08.037`, `arXiv:hep-ph/0512210`.

[73] M. Cacciari, G. P. Salam, and G. Soyez, "FastJet user manual", *Eur. Phys. J. C* **72** (2012) 1896, `doi:10.1140/epjc/s10052-012-1896-2`, `arXiv:1111.6097`.

[74] **CMS** Collaboration, "Determination of jet energy calibration and transverse momentum

resolution in CMS", *JINST* **6** (2011) P11002, doi:10.1088/1748-0221/6/11/P11002, arXiv:1107.4277.

[75] **CMS** Collaboration, "Pileup Jet Identification", CMS Physics Analysis Summary CMS-PAS-JME-13-005, CERN, 2013.

[76] **CMS** Collaboration, "Jet algorithms performance in 13 TeV data", CMS Physics Analysis Summary CMS-PAS-JME-16-003, CERN, 2017.

[77] D. Guest et al., "Jet Flavor Classification in High-Energy Physics with Deep Neural Networks", *Phys. Rev. D* **94** (2016), no. 11, 112002, doi:10.1103/PhysRevD.94.112002, arXiv:1607.08633.

[78] **CMS** Collaboration, "Identification of heavy-flavour jets with the CMS detector in pp collisions at 13 TeV", *JINST* **13** (2018), no. 05, P05011, doi:10.1088/1748-0221/13/05/P05011, arXiv:1712.07158.

[79] **CMS** Collaboration, "Performance of missing energy reconstruction in 13 TeV pp collision data using the CMS detector", CMS Physics Analysis Summary CMS-PAS-JME-16-004, CERN, 2016.

[80] **CMS** Collaboration, "Performance of missing transverse momentum in pp collisions at $\sqrt{s} = 13$ TeV using the CMS detector", CMS Physics Analysis Summary CMS-PAS-JME-17-001, CERN, 2018.

[81] **SLAC** Collaboration, "Simulations". https://theory.slac.stanford.edu/our-research/simulations. (Retrieved Jul 25, 2017).

[82] **CMS** Collaboration, "Event generator tunes obtained from underlying event and multiparton scattering measurements", *Eur. Phys. J. C* **76** (2016) 155, doi:10.1140/epjc/s10052-016-3988-x, arXiv:1512.00815.

[83] **CMS** Collaboration, "Extraction and validation of a new set of CMS PYTHIA8 tunes from underlying-event measurements", *Eur. Phys. J. C* **80** (2020) 4, doi:10.1140/epjc/s10052-019-7499-4, arXiv:1903.12179.

[84] **CMS** Collaboration, "Investigations of the impact of the parton shower tuning in Pythia 8 in the modelling of $t\bar{t}$ at $\sqrt{s} = 8$ and 13 TeV", CMS Physics Analysis Summary CMS-PAS-TOP-16-021, CERN, 2016.

[85] **GEANT4** Collaboration, "GEANT4 — a simulation toolkit", *Nucl. Instrum. Meth. A* **506** (2003) 250, doi:10.1016/S0168-9002(03)01368-8.

[86] M. H. Seymour and M. Marx, "Monte Carlo Event Generators", in *Proceedings, 69th Scottish Universities Summer School in Physics: LHC Phenomenology (SUSSP69) 2012*, p. 287. St.Andrews, Scotland, U.K., 2013. arXiv:1304.6677. doi:10.1007/978-3-319-05362-2_8.

[87] T. Sjöstrand, S. Mrenna, and P. Z. Skands, "PYTHIA 6.4 Physics and Manual", *JHEP* **05** (2006) 026, doi:10.1088/1126-6708/2006/05/026, arXiv:hep-ph/0603175.

[88] F. Maltoni and T. Stelzer, "MadEvent: Automatic event generation with MadGraph", *JHEP* **02** (2003) 027, doi:10.1088/1126-6708/2003/02/027, arXiv:hep-ph/0208156.

[89] J. Alwall et al., "Comparative study of various algorithms for the merging of parton showers and matrix elements in hadronic collisions", *Eur. Phys. J. C* **53** (2008) 473, doi:10.1140/epjc/s10052-007-0490-5, arXiv:0706.2569.

[90] J. Alwall et al., "The automated computation of tree-level and next-to-leading order differential cross sections, and their matching to parton shower simulations", *JHEP* **07** (2014) 079, doi:10.1007/JHEP07(2014)079, arXiv:1405.0301.

[91] P. Nason, "A new method for combining NLO QCD with shower Monte Carlo algorithms", *JHEP* **11** (2004) 040, doi:10.1088/1126-6708/2004/11/040, arXiv:hep-ph/0409146.

[92] S. Frixione, P. Nason, and C. Oleari, "Matching NLO QCD computations with parton shower simulations: the POWHEG method", *JHEP* **11** (2007) 070, doi:10.1088/1126-6708/2007/11/070, arXiv:0709.2092.

[93] S. Alioli, P. Nason, C. Oleari, and E. Re, "A general framework for implementing NLO calculations in shower Monte Carlo programs: the POWHEG BOX", *JHEP* **06** (2010) 043, doi:10.1007/JHEP06(2010)043, arXiv:1002.2581.

[94] S. Frixione, P. Nason, and G. Ridolfi, "A positive-weight next-to-leading-order Monte Carlo for heavy flavour hadroproduction", *JHEP* **09** (2007) 126, doi:10.1088/1126-6708/2007/09/126, arXiv:0707.3088.

[95] J. M. Campbell, R. K. Ellis, P. Nason, and E. Re, "Top-Pair Production and Decay at NLO Matched with Parton Showers", *JHEP* **04** (2015) 114, doi:10.1007/JHEP04(2015)114, arXiv:1412.1828.

[96] S. Alioli, P. Nason, C. Oleari, and E. Re, "NLO single-top production matched with shower in POWHEG: s- and t-channel contributions", *JHEP* **09** (2009) 111, doi:10.1088/1126-6708/2009/09/111, arXiv:0907.4076. [Erratum: doi:10.1007/JHEP02(2010)011].

[97] E. Re, "Single-top Wt-channel production matched with parton showers using the POWHEG method", *Eur. Phys. J. C* **71** (2011) 1547, doi:10.1140/epjc/s10052-011-1547-z, arXiv:1009.2450.

[98] T. Sjöstrand, S. Mrenna, and Z. S., Peter, "A Brief Introduction to PYTHIA 8.1", *Comput. Phys. Commun.* **178** (2008) 852, doi:10.1016/j.cpc.2008.01.036, arXiv:0710.3820.

[99] T. Sjöstrand et al., "An introduction to PYTHIA 8.2", *Comput. Phys. Commun.* **191** (2015) 159, doi:10.1016/j.cpc.2015.01.024, arXiv:1410.3012.

[100] R. D. Ball et al., "Parton distributions for the LHC Run II", *JHEP* **15** (2015) 40, doi:10.1007/JHEP04(2015)040, arXiv:1410.8849.

[101] K. Melnikov and F. Petriello, "Electroweak gauge boson production at hadron colliders through O(alpha(s)**2)", *Phys.Rev. D* **74** (2006) 114017, doi:10.1103/PhysRevD.74.114017, arXiv:hep-ph/0609070.

[102] M. Czakon and A. Mitov, "Top++: A Program for the Calculation of the Top-Pair Cross-Section at Hadron Colliders", *Comput. Phys. Commun.* **185** (2014) 2930, doi:10.1016/j.cpc.2014.06.021, arXiv:1112.5675.

[103] "NNLO+NNLL top-quark-pair cross sections – ATLAS-CMS recommended predictions for top-quark-pair cross sections using the Top++v2.0 program (M. Czakon, A. Mitov, 2013)", https://twiki.cern.ch/twiki/bin/view/LHCPhysics/TtbarNNLO, 2022. (Retrieved Dec 21, 2020).